



Published in final edited form as:

*Acad Radiol.* 2007 December ; 14(12): 1441–1447. doi:10.1016/j.acra.2007.09.016.

## Noninvasive Differentiation of Uric Acid versus Non-Uric Acid Kidney Stones Using Dual-Energy CT

**Andrew N. Primak, Joel G. Fletcher, Terri J. Vrtiska, Oleksandr P. Dzyubak, John C. Lieske, Molly E. Jackson, James C. Williams Jr, and Cynthia H. McCollough**

CT Clinical Innovation Center, Department of Radiology (A.N.P., J.G.F., T.J.V., O.P.D., C.H.M.) and Division of Nephrology and Hypertension, Department of Internal Medicine (J.C.L.), Mayo Clinic College of Medicine, 200 First Street SW, Rochester, MN 55905; Department of Anatomy and Cell Biology, Indiana University School of Medicine, Indianapolis, IN (M.E.J., J.C.W.)

### Abstract

**Rationale and Objectives**—To determine the accuracy and sensitivity for dual-energy computed tomography (DECT) discrimination of uric acid (UA) stones from other (non-UA) renal stones in a commercially implemented product.

**Materials and Methods**—Forty human renal stones comprising uric acid ( $n = 16$ ), hydroxyapatite ( $n = 8$ ), calcium oxalate ( $n = 8$ ), and cystine ( $n = 8$ ) were inserted in four porcine kidneys (10 each) and placed inside a 32-cm water tank anterior to a cadaver spine. Spiral dual-energy scans were obtained on a dual-source, 64-slice computed tomography (CT) system using a clinical protocol and automatic exposure control. Scanning was performed at two different collimations (0.6 mm and 1.2 mm) and within three phantom sizes (medium, large, and extra large) resulting in a total of six image datasets. These datasets were analyzed using the dual-energy software tool available on the CT system for both accuracy (number of stones correctly classified as either UA or non-UA) and sensitivity (for UA stones). Stone characterization was correlated with micro-CT.

**Results**—For the medium and large phantom sizes, the DECT technique demonstrated 100% accuracy (40/40), regardless of collimation. For the extra large phantom size and the 0.6-mm collimation (resulting in the noisiest dataset), three (two cystine and one small UA) stones could not be classified (93% accuracy and 94% sensitivity). For the extra large phantom size and the 1.2-mm collimation, the dual-energy tool failed to identify two small UA stones (95% accuracy and 88% sensitivity).

**Conclusions**—In an anthropomorphic phantom model, dual-energy CT can accurately discriminate uric acid stones from other stone types.

### Keywords

Kidney stones; renal calculi; dual-energy computed tomography; uric acid; urolithiasis

---

Symptomatic urinary stone disease affects approximately 900,000 persons in the United States each year, resulting in annual medical cost of \$5.3 billion. Nephrolithiasis has traditionally been evaluated using plain film radiographic techniques with or without tomography or administration of intravenous contrast for excretory urography. Over recent years, however, computed tomography (CT) has supplanted these traditional techniques because of increased sensitivity, speed, and the lack of intravenous contrast (1). Furthermore, improved CT

acquisition techniques can allow a lower radiation dose than was required for a traditional excretory urogram (2,3).

Although state-of-the-art CT provides accurate submillimeter details of the size and location of renal stones (4,5), current routine clinical image analysis does not differentiate stone composition. This is particularly important in the case of uric acid (UA) stones (~10% of cases), because urinary alkalinization can be prescribed to dissolve UA stones and could thereby be initiated at presentation rather than following lengthy metabolic workup. Therefore simple and reliable differentiation of UA versus non-UA stone composition could potentially allow patients with UA stones to avoid invasive interventional urinary procedures for stone removal or external shock wave lithotripsy, both of which are expensive and might result in renal hemorrhage, fibrosis, or hypertension (6).

Previous attempts to predict stone composition using spiral CT were based on the analysis of CT numbers. Several in vitro and in vivo studies have shown that this approach can discriminate UA from non-UA stones (7-11). Combining the analysis of CT numbers with visual assessment of stone morphology using a wide window setting (eg, bone window) substantially improves the accuracy of stone characterization (12). Bellin et al (13) reported in vitro prediction of stone composition with 64%-81% accuracy, whereas Zarse et al (14) demonstrated that high-resolution spiral CT yields unique CT numbers for common types of stones if proper window settings are used to localize homogeneous regions within the stones.

However, the CT number approach to predict stone composition is not yet robust or reliable enough to be used as a routine clinical application, and a dual-energy CT (DECT) technique could be considered as an alternative. Because UA stones are composed only of light chemical elements (H, C, N, O), their x-ray attenuation properties at high and low kVp are very different compared with those for other (non-UA) stone types (eg, calcium oxalate, calcium hydroxyapatite, cystine), whose composition includes heavy elements (P, Ca, S). As a consequence, UA stones have higher CT numbers at higher kVp than at lower kVp, whereas non-UA stones have higher CT numbers at lower kVp than at higher kVp. Indeed, some previous studies (8,13,15) have already exploited this fact and used the difference between CT numbers at high and low kVp to improve the prediction accuracy of the CT number approach.

A recently introduced dual-source CT scanner (SOMATOM Definition, Siemens Medical Solutions, Forchheim, Germany) allows simultaneous dual-energy, high spatial resolution acquisition and immediate image postprocessing using a commercial material decomposition algorithm (SyngoDE, Siemens). Our previous study (16), which used both single-source and preliminary dualsource CT data analyzed with the beta version of the material decomposition software, demonstrated 75%-100% accuracy of the DECT technique in differentiating UA from non-UA stones. Several recent software and hardware upgrades have improved both the scanner performance and the material decomposition algorithm. Therefore the current study was undertaken to demonstrate the in vitro prediction accuracy of the DECT system to differentiate UA from non-UA stones under clinical conditions.

## MATERIALS AND METHODS

Forty urinary stones (Fig 1) of different composition and size that were passed or removed from human patients and had been previously characterized with infrared spectroscopy were obtained from the Mayo Clinic Metals Laboratory. Four different stone types were selected: uric acid (16 stones), calcium oxalate monohydrate (8 stones), hydroxyapatite (8 stones), and cystine (8 stones). Stone sizes varied from 2 to 7 mm, with 12 "small" stones (6 UA stones) being smaller than approximately 3 mm in size.

The stones were hydrated to make sure all pores were filled with water and inserted in four bivalved porcine kidneys (10 stones each kidney). The kidneys with stones were placed in a 32-cm water tank anterior to a cadaver spine to create realistic scattering and attenuation conditions. To take into account variable patient attenuation, we simulated three patient sizes: half-full water tank (medium), full water tank (large), and full water tank with extra attenuating material (Superflab, Radiation Product Design, Inc, Albertville, MN) wrapped around it (extra large).

Spiral scanning was performed on the dual-source CT scanner using a clinical dual-energy protocol and automatic exposure control (CAREdose4D, Siemens). The following acquisition parameters were used: tube A at 140 kVp and 100 quality reference mAs, tube B at 80 kVp and 425 quality reference mAs (this high value for quality reference mAs resulted in maximum tube B current for all phantom sizes, whereas the tube A current was adjusted with the phantom size by automatic exposure control), 0.7 pitch, and 0.5 second rotation time. Two acquisitions were performed for each phantom size. One was carried out using  $2 \times 32 \times 0.6$  mm collimation with z-flying focal spot (resulting in 64 overlapped slices) and another with  $14 \times 1.2$  mm collimation. Therefore a total of six dual-energy scans were acquired. The volume CT dose index values for all scans, which were set to match our clinically routine abdominal/pelvis volume CT dose index values, are summarized in Table 1. Two series of images (80 and 140 kVp) were reconstructed for each scan using a 200-mm field of view and a D30 kernel. The  $2 \times 32 \times 0.6$  mm data were reconstructed using 1.0-mm image thickness and 0.8-mm reconstruction interval, whereas 1.5-mm image thickness and 1.0 mm reconstruction interval were used for the  $14 \times 1.2$  mm data. The approximate noise levels measured inside the kidneys for all image datasets are also summarized in Table 1.

The reconstructed 80 and 140 kVp images were analyzed using a commercially available software tool ("Kidney Stones," Syngo DE Viewer, Siemens), which uses a three-material decomposition algorithm. According to this algorithm, a kidney stone can be considered as a mixture of a hypothetical "pure" stone with no pores (such a stone would have unrealistically high CT numbers) and the material that fills the pores ("urine"). In a plot of the CT numbers at 80 kVp versus the CT numbers at 140 kVp, a real stone has to lie somewhere (depending on its porosity) on a line segment between the "urine" and the "pure" stone datapoints (Fig 2). In this approach, each stone type is characterized by its own slope in the dual-energy CT number plot, which is determined using stones of known composition. Because UA stones are made of light chemical elements, their slope is quite different (Fig 2) from the slopes of non-UA stones, which have heavier atoms. As the slopes of non-UA stones are relatively close to each other and overlap when error bars are taken into account, they are represented in Fig 2 by a single average slope corresponding to all non-UA stones. Figure 2 also provides a simplified picture of how the dual-energy algorithm works. If a datapoint corresponding to a stone with unknown composition falls below the angle bisector (dashed line) dividing the angle between the UA and non-UA line segments, the algorithm will characterize such stone as a UA stone (open circle in Fig 2) and assign it a predefined color code (red in Fig 3). If an unknown datapoint falls above the angle bisector, the corresponding stone will be identified as a non-UA stone (gray circle in Fig 2) and assigned a different predefined color code (blue in Fig 3). Examples of the color-coded images from our study produced by the dual-energy software tool are presented in Fig 3. After the dual-energy analysis was completed, both accuracy (number of stones correctly classified as either UA or non-UA) and sensitivity (number of UA stones classified as UA) were determined for all six datasets.

After the completion of the experiment, the stones were dried, and evaluation of the internal structure of all stones was performed using micro CT. Each stone was scanned on a Scanco mCT20 micro-CT system (Scanco Medical AG, Bassersdorf, Switzerland) with 18- $\mu$ m isotropic voxel size and assessed for stone composition, as previously described (17). The goal

of this additional characterization was to find out if any of the stones previously identified by infrared spectroscopy as “pure” showed evidence of a mixed composition. Examples of micro-CT sections of the stones used in this study are shown in Fig 4. For the stones with mixed composition, the volume content of each mineral component was estimated using ImageJ (a public domain image processing program) by thresholding the stone images at levels appropriate for the individual minerals (17). Stones were analyzed by micro-CT blindly; that is, the micro-CT analyses were completed without knowledge of the infrared spectroscopy data.

## RESULTS

The dual-energy stone characterization results are summarized in Table 2. For the medium and large phantom sizes, the dual-energy software tool correctly identified all 40 stones as either UA or non-UA, regardless of the detector collimation, demonstrating 100% accuracy and 100% sensitivity.

For the extra large phantom size and the 0.6-mm collimation, three stones could not be classified, resulting in 93% accuracy (37/40) and 94% sensitivity (15/16). One small UA stone (UA #14) was not color-coded at all and two cystine stones (cystine #1 and cystine #3) were assigned both colors. This dataset had the largest amount of noise at 80 kVp.

For the extra large phantom size and the 1.2-mm collimation, the dual-energy tool failed to identify two small UA stones (UA #14 and UA #16), demonstrating 95% accuracy (38/40) and 88% sensitivity. The remainder of the small (<3 mm) UA stones were identified as UA stones resulting in 67% (4/6) sensitivity.

For all stones, micro-CT confirmed the major mineral compositions as determined by infrared spectroscopy. However, micro-CT revealed visible content of other minerals in many of the stones; this is expected, because most stones contain more than one mineral component (18). In particular, micro-CT revealed calcium salt content in 13 of the 16 uric acid stones. However, this content was quite minor (<2% by volume) in all cases. The micro-CT scans of the stones inaccurately characterized in the extra large phantom did not reveal any obvious reasons for the inaccurate identification by the dual-energy method. One of the two cystine stones was noted to be quite porous, which would reduce the overall x-ray attenuation within that stone, and the other had a small speck of apatite. However, other cystine stones were equally porous yet were identified correctly, and a speck of apatite should have aided classification of this stone as non-UA. Both of the UA stones inaccurately classified were quite small and contained scattered regions of calcium salts, so that the combination of these two features may have contributed to their misidentification in the extra large phantom.

## DISCUSSION

Our results demonstrate that the three-material decomposition algorithm can accurately discriminate between UA and other stone types. For stones larger than 3 mm in size, using a clinical dual-energy protocol with the  $14 \times 1.2$  mm collimation resulted in 100% accuracy of UA versus non-UA characterization, even for the largest phantom size, when the images acquired with 80 kVp were very noisy. For stones smaller than approximately 3 mm in size, the accuracy of the dual-energy technique was at least 92% (11/12) when the  $32 \times 0.6$  mm collimation was used. Stone characterization can be obtained immediately after the scan by running the dual-energy software tool available on the system, with a processing time of 1-2 minutes or less.

The performance of the dual-energy technique in extra large patients is hampered by two factors. First, the 80-kVp images become extremely noisy, increasing error bars for the

datapoints representing the stones in the dual-energy plot. A stone whose datapoint is located relatively close to the angle bisector might have error bars which extend beyond the bisector line separating UA from non-UA stones. Such a stone cannot be confidently classified as a UA or non-UA stone, resulting in algorithm failure. The second factor is beam hardening, which is more evident in extra large patients. Strong beam hardening can modify the CT numbers, both at 80 and 140 kVp, and, hence, change the stone's position in the dual-energy plot, bringing it closer to the angle bisector line. The dual-energy algorithm's failure to identify two cystine stones in the extra large phantom scanned with the  $32 \times 0.6$  mm collimation (the noisiest dataset) was most likely caused by the combined effect of these two factors. Despite these considerations, the dual-energy technique correctly identified all stones  $>3$  mm under all conditions.

One of the advantages of the dual-energy material decomposition algorithm is that it is not strongly affected by the partial volume artifact. The voxels at the periphery of a stone are partially filled with the stone material and partially with the material surrounding the stone (urine). If we represent each voxel as a point in the dual-energy plot, the periphery voxels fall on the same line segment (connecting the "urine" and "pure" stone points, as shown in Fig 2) as the voxels inside the stone, which are also partially filled with urine occupying the pores. The points corresponding to the two voxels would simply be at different distances from the "pure" stone end of the line segment. Therefore both the periphery and inside voxels lie on the same line segment, the slope of which determines their composition. Thus partial volume averaging does not play as significant role in the dual-energy algorithm as it does in stone characterization techniques based on the CT numbers. These techniques are strongly dependent on the partial volume artifact (19,20) because the CT numbers of the periphery voxels are quite different from the CT numbers inside the stone.

Because all aspects of the study design were carefully chosen to simulate a clinical setting as much as possible, we expect similar performance of the dual-energy technique in vivo. The primary clinical limitation will be a less than 100% accuracy for identifying small stones ( $<3$  mm) in very large patients.

In conclusion, we have demonstrated in a realistic phantom model that a dual-energy stone characterization technique can discriminate UA stones from other stone types with 92%-100% accuracy, depending on stone size and patient attenuation. Similar accuracy is anticipated in vivo. This algorithm addresses an important clinical need for identifying UA stones on abdominal/pelvic CT scans, the predominant tool used to diagnose and stage renal stones.

## ACKNOWLEDGMENTS

The authors would like to thank Ms. Kristina Nunez for assistance with manuscript submission.

## REFERENCES

1. Kawashima A, Vrtiska TJ, LeRoy AJ, et al. CT urography. *Radiographics* 2004;24(Suppl 1):S35–S58. [PubMed: 15486248]
2. Kalra MK, Maher MM, D'Souza RV, et al. Detection of urinary tract stones at low-radiation-dose CT with z-axis automatic tube current modulation: phantom and clinical studies. *Radiology* 2005;235:523–529. [PubMed: 15770037]
3. Heneghan JP, McGuire KA, Leder RA, et al. Helical CT for nephrolithiasis and ureterolithiasis: comparison of conventional and reduced radiation-dose techniques. *Radiology* 2003;229:575–580. [PubMed: 14526095]
4. Williams JC Jr, Kim SC, Zarse CA, et al. Progress in the use of helical CT for imaging urinary calculi. *J Endourol* 2004;18:937–941. [PubMed: 15801357]
5. Vrtiska TJ. Quantitation of stone burden: imaging advances. *Urol Res* 2005;33:398–402.

6. Evan AP, Willis LR, Lingeman JE, et al. Renal trauma and the risk of longterm complications in shock wave lithotripsy. *Nephron* 1998;78:1–8. [PubMed: 9453396]
7. Joseph P, Mandal AK, Singh SK, et al. Computerized tomography attenuation value of renal calculus: can it predict successful fragmentation of the calculus by extracorporeal shock wave lithotripsy? A preliminary study. *J Urol* 2002;167:1968–1971.
8. Mostafavi MR, Ernst RD, Saltzman B. Accurate determination of chemical composition of urinary calculi by spiral computerized tomography. *J Urol* 1998;159:673–675. [PubMed: 9474123]
9. Motley G, Dalrymple N, Keesling C, et al. Hounsfield unit density in the determination of urinary stone composition. *Urology* 2001;58:170–173. [PubMed: 11489691]
10. Nakada SY, Hoff DG, Attai S, et al. Determination of stone composition by noncontrast spiral computed tomography in the clinical setting. *Urology* 2000;55:816–819. [PubMed: 10840083]
11. Pareek G, Armenakas NA, Fracchia JA. Hounsfield units on computerized tomography predict stone-free rates after extracorporeal shock wave lithotripsy. *J Urol* 2003;169:1679–1681. [PubMed: 12686807]
12. Williams JC Jr, Paterson RF, Kopecky KK, et al. High resolution detection of internal structure of renal calculi by helical computerized tomography. *J Urol* 2002;167:322–326. [PubMed: 11743350]
13. Bellin MF, Renard-Penna R, Conort P, et al. Helical CT evaluation of the chemical composition of urinary tract calculi with a discriminant analysis of CT-attenuation values and density. *Eur Radiol* 2004;14:2134–2140. [PubMed: 15221262]
14. Zarse CA, McAteer JA, Tann M, et al. Helical computed tomography accurately reports urinary stone composition using attenuation values: in vitro verification using high-resolution micro-computed tomography calibrated to fourier transform infrared microspectroscopy. *Urology* 2004;63:828–833. [PubMed: 15134957]
15. Mitcheson HD, Zamenhof RG, Bankoff MS, et al. Determination of the chemical composition of urinary calculi by computerized tomography. *J Urol* 1983;130:814–819. [PubMed: 6887427]
16. Primak, AN.; Fletcher, JG.; Krauss, B., et al. Non-invasive prediction of renal stone composition using high spatial resolution, dual-energy CT. *Radiol Soc North Am Scient Assembly Annu Meeting*; 2006. p. 753
17. Zarse CA, McAteer JA, Sommer AJ, et al. Nondestructive analysis of urinary calculi using micro computed tomography. *BMC Urol* 2004;4:15. [PubMed: 15596006]
18. Daudon M, Donsimoni R, Hennequin C, et al. Sex-and age-related composition of 10 617 calculi analyzed by infrared spectroscopy. *Urol Res* 1995;23:319–326. [PubMed: 8839389]
19. Saw KC, McAteer JA, Monga AG, et al. Helical CT of urinary calculi: effect of stone composition, stone size, and scan collimation. *AJR Am J Roentgenol* 2000;175:329–332. [PubMed: 10915668]
20. Williams JC Jr, Saw KC, Monga AG, et al. Correction of helical CT attenuation values with wide beam collimation: in vitro test with urinary calculi. *Acad Radiol* 2001;8:478–483. [PubMed: 11394540]

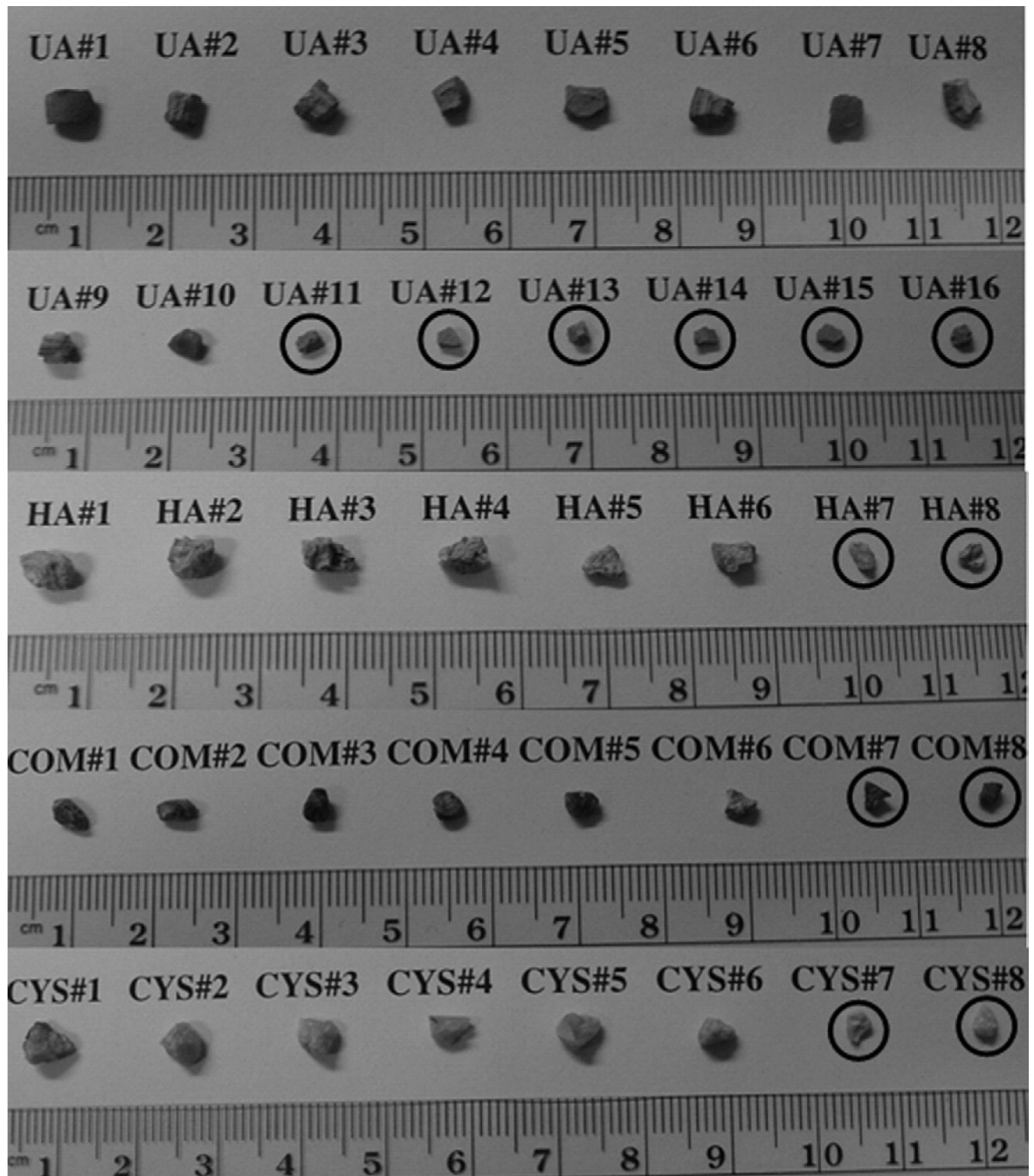


**Figure 1.**  
Forty human renal stones used in this study. The 12 “small” stones smaller than approximately 3 mm in size are circled.

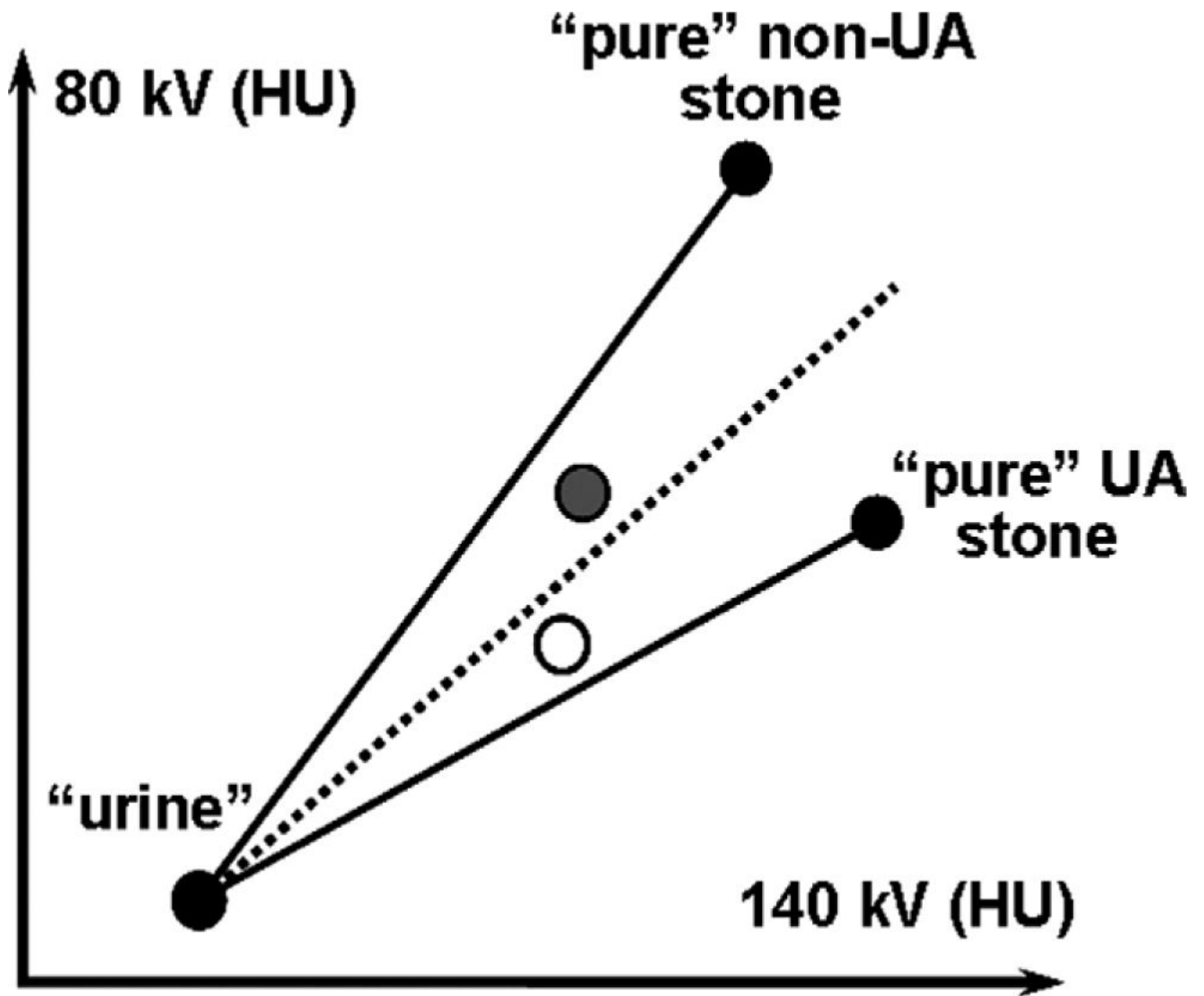


**Figure 2.**

A simplified description of how the DE algorithm works. If a datapoint corresponding to a stone with unknown composition falls below the bisector line (dashed) dividing the angle between the uric acid (UA) and non-UA line segments, the algorithm will characterize such stone as a UA stone (open circle). If an unknown datapoint falls above the angle bisector line, the corresponding stone will be identified as a non-UA stone (gray circle).

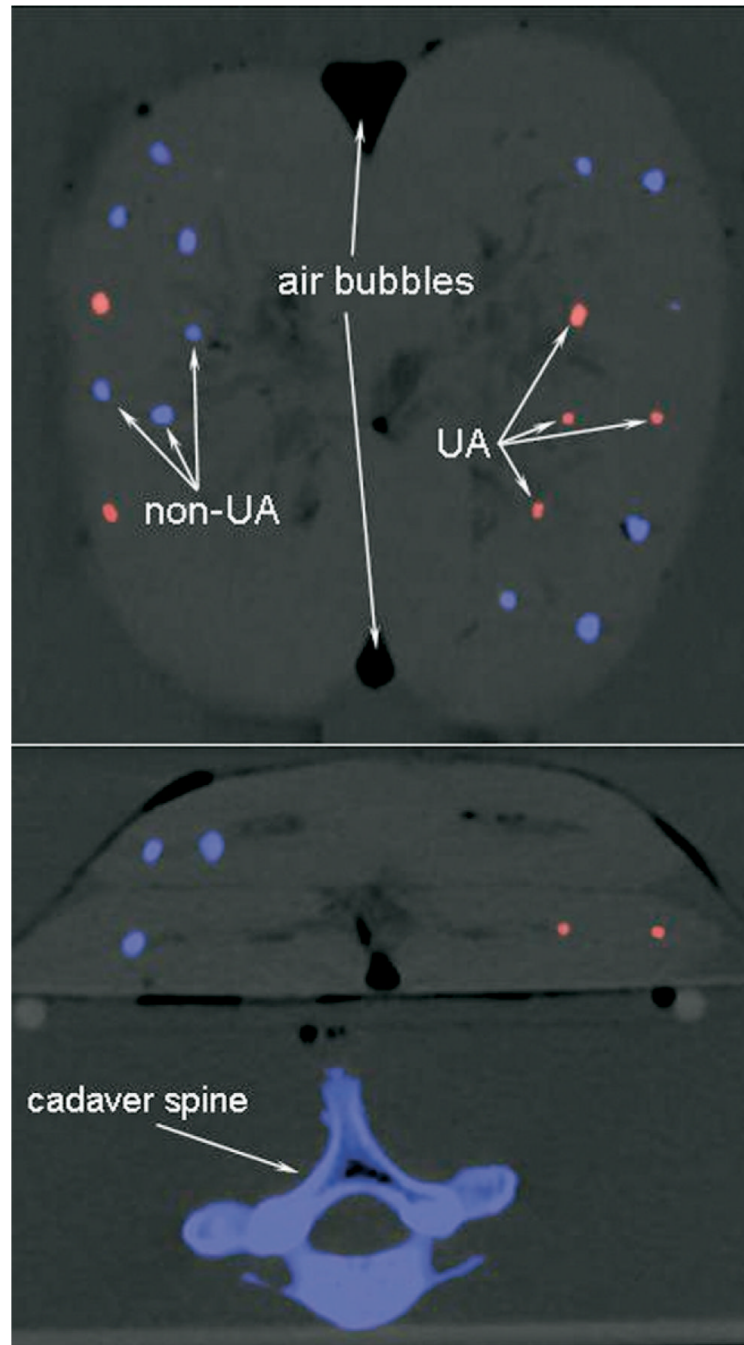


**Figure 3.** Examples of the color-coded images produced by the dual-energy software tool (Kidney Stones, Syngo DE Viewer, Siemens).

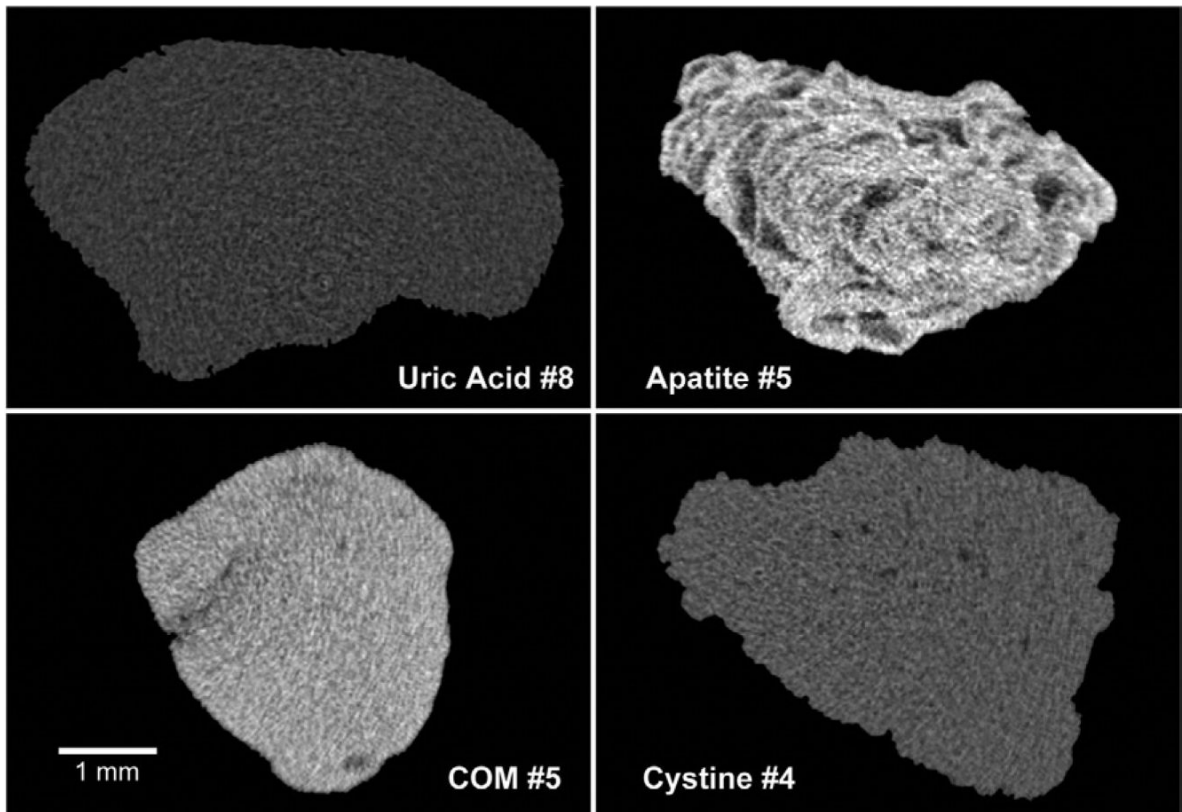


**Figure 4.** Micro-computed tomography slices showing the four types of stone used in this study and their generally homogeneous nature. Uric acid and cystine stones are generally the purest of the stones, with the uniform shade of gray in the examples shown here indicating such purity. The dark spots in the cystine stone (lower right) indicate the presence of void regions, which are common in this stone type. The layered nature of the apatite stone (upper right) is typical of this stone type, and the lower attenuation layers (darker gray) often contain calcium oxalate. The calcium oxalate monohydrate (COM) example (lower left) shows the typical uniform distribution of mineral in this stone type, with some void regions indicated by the darker grays.

**Table 1**

The Dose and Noise Levels for Different Phantom Sizes

Phantom	Medium Size			Large Size			Extra Large Size		
	$2 \times 32 \times 0.6$	$14 \times 1.2$	$14 \times 1.2$	$2 \times 32 \times 0.6$	$15.3$	$14 \times 1.2$	$2 \times 32 \times 0.6$	$21.9$	$14 \times 1.2$
Collimation	14.0	13.7	15.0	34	27	30	64	25	51
Dose (volume CT dose index) (mGy)	18	15	17	21	17	21	21	21	21
Noise (Hounsfield units) at 80 kVp									
Noise (Hounsfield units) at 80 kVp									

**Table 2**  
Accuracy and Sensitivity of Renal Stone Characterization with the New Dual-Energy Material Decomposition Algorithm

Experiment	Accuracy*			Sensitivity <sup>†</sup>		
	All Stones	Large Stones	Small Stones <sup>‡</sup>	All Stones	Large Stones	Small Stones <sup>‡</sup>
Medium size	100%	100%	100%	100%	100%	100%
Both collimations	(40/40)	(28/28)	(12/12)	(16/16)	(10/10)	(6/6)
Large size	100%	100%	100%	100%	100%	100%
Both collimations	(40/40)	(28/28)	(12/12)	(16/16)	(10/10)	(6/6)
Extra large size	93%	93%	92%	94%	100%	83%
2 × 32 × 0.6 mm	(37/40)	(26/28)	(11/12)	(15/16)	(10/10)	(5/6)
Extra large size	95%	100%	83%	88%	100%	67%
14 × 1.2 mm	(38/40)	(28/28)	(10/12)	(14/16)	(10/10)	(4/6)

\* Number of stones correctly classified as either uric acid or non-uric acid.

<sup>†</sup> Number of uric acid stones correctly classified as uric acid.

<sup>‡</sup> Approximately smaller than 3 mm in size.